J. Micromech. Microeng. **6** (1996) 320–329. Printed in the UK

Comb-drive actuators for large displacements

Rob Legtenberg, A W Groeneveld and M Elwenspoek

MESA Research Institute, University of Twente, PO Box 217, 7500 AE Enschede, The Netherlands

Received 30 November 1995, accepted for publication 4 June 1996

Abstract. The design, fabrication and experimental results of lateral-comb-drive actuators for large displacements at low driving voltages is presented. A comparison of several suspension designs is given, and the lateral large deflection behaviour of clamped–clamped beams and a folded flexure design is modelled. An expression for the axial spring constant of folded flexure designs including bending effects from lateral displacements, which reduce the axial stiffness, is also derived. The maximum deflection that can be obtained by comb-drive actuators is bounded by electromechanical side instability. Expressions for the side-instability voltage and the resulting displacement at side instability are given. The electromechanical behaviour around the resonance frequency is described by an equivalent electric circuit. Devices are fabricated by polysilicon surface micromachining techniques using a one-mask fabrication process. Static and dynamic properties are determined experimentally and are compared with theory. Static properties are determined by displacement-to-voltage, capacitance-to-voltage and pull-in voltage measurements. Using a one-port approach, dynamic properties are extracted from measured admittance plots. Typical actuator characteristics are deflections of about 30 μm at driving voltages around 20 V, a resonance frequency around 1.6 kHz and a quality factor of approximately 3.

1. Introduction

Comb drive actuators consist of two interdigitated finger structures, where one comb is fixed and the other is connected to a compliant suspension. Applying a voltage difference between the comb structures will result in a deflection of the movable comb structure by electrostatic forces. Comb drive actuators have been used as resonators [1–3], electromechanical filters [4], optical shutters [5–7], microgrippers [8] and voltmeters [9]. They have also been used as the driving element in, e.g. vibromotors [10] and micromechanical gears [11].

Voltage controlled comb-drive actuators exert a lateral electrostatic force which is independent of position making them attractive for micropositioning applications, such as, for instance, xy-microstages [12–14]. Together with nanotools like microtips, integrated systems can be fabricated with applications in scanning microscopy and data storage [15, 16]. In most devices actuator deflections have been limited to a few microns but in many cases micropositioning over larger distances is attractive. For this reason the design and fabrication of large displacement comb-drive actuators is investigated.

A suspension that is compliant in the direction of displacement desired and stiff in the orthogonal directions is required. Electrostatic forces increase with decreasing gap spacing and an increasing number of comb fingers. However, due to fabrication processes, dimensions are limited by minimum feature size constraining, e.g., the minimum beam width and gap spacing. These and other design constraints are discussed in order to obtain large-displacement, low-driving-voltage comb-drive actuators.

2. Spring designs

Different types of spring designs have been applied in comb-drive actuators [1, 12, 17]. In this section the following spring designs will be discussed; clamped–clamped beams, a crab-leg flexure and the folded-beam flexure. In most cases it is desirable to have a structure which is very compliant in one direction while being very stiff in the orthogonal directions. This can be expressed as a stiffness ratio. Most polysilicon micromechanical flexures constrain motion to a rectilinear direction, and are created from straight beams. When a concentrated load is applied the linear spring constant is defined as

$$k_i = \frac{F_i}{\delta_i} \tag{1}$$

where F_i and δ_i are respectively the force and the deflection in the i direction. The lateral spring constants and stiffness ratio of a clamped–clamped beam, a crab-leg flexure and a folded flexure design will be discussed. The analysis assumes that there is no residual stress present in the spring structures.

0960-1317/96/030320+10$19.50

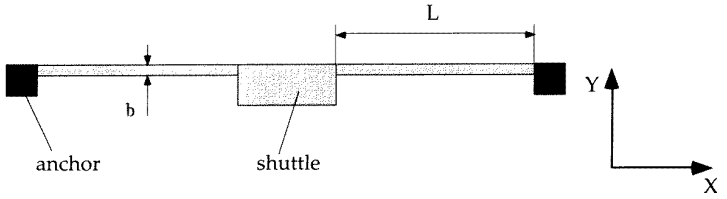

Figure 1. Fixed–fixed beam.

2.1. Clamped–clamped beam

A clamped–clamped beam with rectangular cross section is shown in figure 1. A concentrated force is applied to the centre of the shuttle. The axial displacement along the x-axis can be found directly from Hooke's law and the lateral displacement along the y-axis is obtained from small deflection theory [18]. The spring constants for a concentrated force in the x- and y-directions are given by:

$$k_x = 2Ebh/L \tag{2}$$

$$k_y = 2Ehb^3/L^3 \tag{3}$$

where E is Young's modulus, b is the beam width, h is the beam thickness and L is the length of one beam segment. The stiffness ratio is:

$$\frac{k_x}{k_y} = \left(\frac{L}{b}\right)^2. \tag{4}$$

The stiffness ratio of a clamped–clamped beam can be very high. For example, the stiffness ratio is 1.25×10^5 for a beam of length 500 μm and width 2 μm. For large displacements, however, extensional axial forces develop in the beam that result in a non-linear force-to-displacement relation. In this case non-linear effects have to be included which strongly increase the stiffness of the beam with increasing deflection. This spring design is therefore not suitable for large deflections. However it is useful in applications that require measurement of axial forces, for instance in order to determine residual stresses or measure externally applied axial stresses as in sensing applications.

A derivation of the large deflection behaviour of clamped–clamped beams can be found in [19]. The centre deflection for a concentrated load P_y at the centre can be found by simultaneously solving the following equations:

$$P_y = \frac{EIh}{L^3}\sqrt{8/3}u^3\left(\frac{3}{2} - \frac{1}{2}\tanh^2 u - \frac{3}{2}\frac{\tanh u}{u}\right)^{-1/2} \tag{5}$$

$$\delta_y = h\sqrt{2/3}(u - \tanh u)\left(\frac{3}{2} - \frac{1}{2}\tanh^2 u - \frac{3}{2}\frac{\tanh u}{u}\right)^{-1/2} \tag{6}$$

with

$$u = \sqrt{N/EI}(L/2) \tag{7}$$

where N is the normal force that develops in the beam as a result of the applied force and I is the second moment of inertia of the beam. The normalised deflection-to-force behaviour is shown in figure 2. This graph shows that the small deflection theory is valid for deflections up to about a quarter of the beam thickness. For larger deflections non-linear theory has to be used.

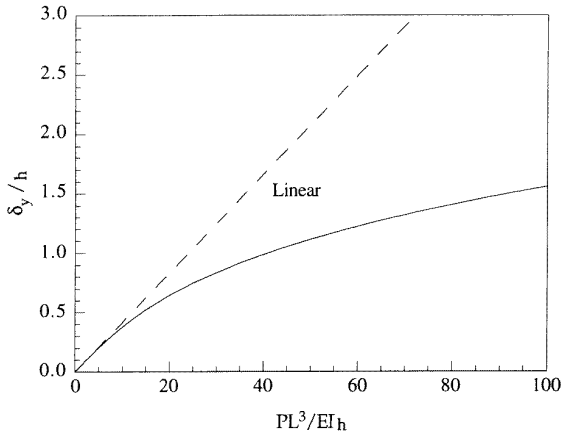

Figure 2. Normalised deflection of a clamped–clamped beam with dimensions ($h \times b \times 2L$) of $5 \times 2 \times 1000$ μm under a force P at the centre.

2.2. Crab-leg flexure

In order to reduce the extensional axial forces a crab-leg flexure can be used. A sketch of a crab-leg flexure is shown in figure 3. The thigh segment has a second moment of inertia I_1 and is of length L_1; the shin segment has a second moment of inertia I_2 and is of length L_2. The spring constants, as a result of a concentrated force on the shuttle, in the x- and y-directions are given by:

$$k_x = \frac{12E_yI_2}{L_2^3}\left\{\frac{L_1I_2 + 2L_2I_1}{2L_1I_2 + L_2I_1}\right\} \tag{8}$$

$$k_y = \frac{24EI_1}{L_1^3}\left\{\frac{L_1I_2 + L_2I_1}{L_1I_2 + 4L_2I_1}\right\}. \tag{9}$$

When the shin and thigh have the same width and thickness, the stiffnes ratio can be obtained from:

$$\frac{k_x}{k_y} = \frac{1}{2}\frac{L_1^3}{L_2^3}\left\{\frac{L_1^2 + 6L_1L_2 + 8L_2^2}{2L_1^2 + 3L_1L_2 + L_2^2}\right\}. \tag{10}$$

Although this design increases the linear deflection region to a certain extent (as will be shown in our measurement results), a large reduction of the stiffness ratio is introduced. A design that has a shin length of 50 μm and thigh dimensions equal to our previous clamped–clamped beam example, has a stiffness ratio that is already several orders of magnitude smaller. A flexure design that is less susceptible to a decrease in the stiffness ratio is the folded flexure design [20].

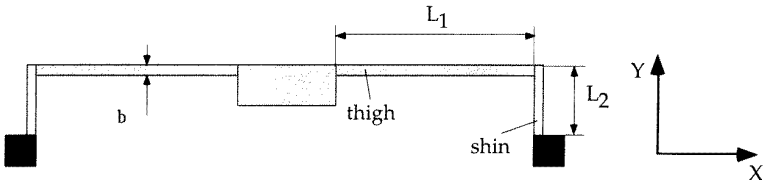

Figure 3. Crab-leg flexure.

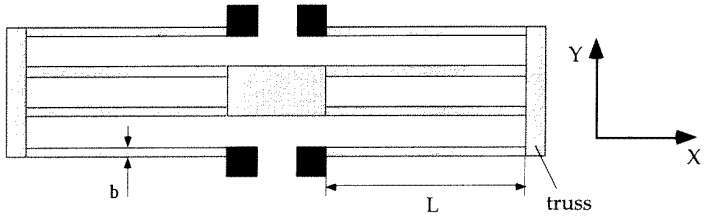

Figure 4. Folded-flexure design.

2.3. Folded flexure

A sketch of the folded beam design is shown in figure 4. The beams are anchored near the centre and the trusses allow expansion or contraction of the beams along the x-axis. Assuming rigid trusses, the spring constant of the folded flexure design in axial and lateral directions can be found from:

$$k_x = 2Ebh/L \tag{11}$$

$$k_y = 2Ehb^3/L^3 \tag{12}$$

and the stiffness ratio is:

$$\frac{k_x}{k_y} = \left(\frac{L}{b}\right)^2. \tag{13}$$

The folded flexure design strongly reduces the development of axial forces and exhibits a much larger linear deflection range. The stiffness ratio for small deflections is equal to the stiffness ratio of a clamped–clamped beam. This design is therefore very suitable for large deflection actuators. For a more extensive analysis of folded beams, including the effect of compliant trusses, the reader is referred to [21] and [22]. The large deflection behaviour of a folded flexure design can be obtained by considering the folded flexure as four folded beams in parallel. Each folded beam is a combination of two clamped–guided beams connected in series. By solving the elastica for a clamped–guided beam the large deflection behaviour of the folded flexure can be described by the following set of equations:

$$\delta_y = 8\sqrt{\frac{EI}{P_y}}\int_{\phi_1}^{\pi/2}\frac{(2p^2\sin\phi - 1)\mathrm{d}\phi}{\sqrt{1-p^2\sin\phi}} \tag{14}$$

where p can be found from numerical iteration and solution of:

$$\frac{1}{4}L\sqrt{\frac{P_y}{EI}} = \int_{\phi_1}^{\pi/2}\frac{\mathrm{d}\phi}{\sqrt{1-p^2\sin^2\phi}} \tag{15}$$

$$\phi_1 = \arcsin\sqrt{2p^2-1}.$$

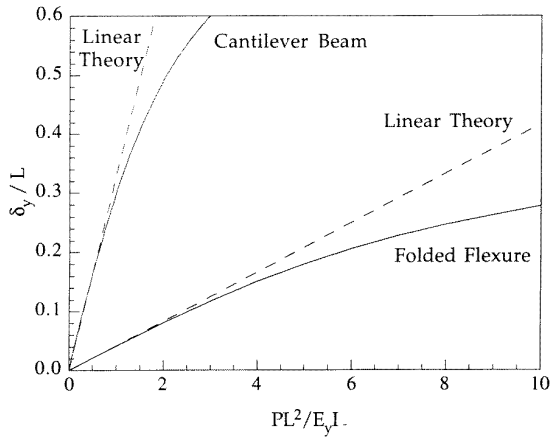

Figure 5. Normalised large deflection behaviour of a beam of length $2L$ that is clamped at one side and guided along the x-axis at the other end, and loaded at it's centre with a concentrated load P. Assuming rigid trusses, such a beam resembles the deflection behaviour of a folded flexure. Also the deflection of a cantilever beam of length L loaded at the tip is shown.

A detailed derivation of these formulae is given in the appendix. In these equations p and ϕ result from a change in variables to bring the equations into the standard form of elliptic integrals. The normalised deflection-to-force behaviour of a folded flexure and cantilever beam is shown in figure 5. The small deflection theory is valid for lateral deflections up to approximately 10% of the beam length, which is considerably larger than in the case of the clamped–clamped beam.

Another important effect that has to be considered is that the stiffness of the folded beam flexure in the x-direction decreases with increasing displacement in the y-direction. Thus, expressions (2), (8) and (11) are in fact upper limits of the axial spring constants at zero

lateral deflection which decrease with increasing lateral deflection. In order to include lateral deflection effects in the axial spring constant of the folded flexure the problem is simplified. Because of the folded beam symmetry only one beam segment is considered. It is assumed that the beam has an initial deflection given by the function $\omega_{0(x)}$. The known admissible trial function of the initial deflection profile is:

$$\omega_{0(x)} = \alpha x^2(6L - 4x). \tag{16}$$

The function of the deflection is approximated by the following admissible trial function:

$$\omega_{(x)} = \beta x^2(6L - 4x) \tag{17}$$

where β is an unknown constant. The total potential energy Π for the beam is:

$$\Pi = \frac{1}{2}EI\int_0^L \left[\frac{\mathrm{d}^2(\omega - \omega_0)}{\mathrm{d}x^2}\right]\mathrm{d}x - P\Delta \tag{18}$$

where P is the axially applied load. The contraction of the beam Δ can be expressed as [23]:

$$\Delta = \frac{1}{2}\int_0^L \left(\frac{\mathrm{d}^2\omega}{\mathrm{d}x^2}\right)^2 \mathrm{d}x - \frac{1}{2}\int_0^L \left(\frac{\mathrm{d}^2\omega_0}{\mathrm{d}x^2}\right)^2 \mathrm{d}x. \tag{19}$$

After extremisation of the potential energy with respect to β, this contraction is given by:

$$\Delta = \frac{3\delta_{\mathrm{beam}}^2}{5L}\left\{\frac{1}{(1 - P/P_{\mathrm{cr}})^2} - 1\right\} \tag{20}$$

where δ_{beam} is the centre deflection of the initial beam curvature and the buckling load P_{cr} is:

$$P_{\mathrm{cr}} = 10EL/L^2. \tag{21}$$

In case of forces that are much smaller than the critical load P_{cr} (i.e. $P/P_{\mathrm{cr}} \ll 1$), the axial deflection of a beam segment can be found from:

$$\Delta = 3PL\delta_{\mathrm{beam}}^2/25EI. \tag{22}$$

The spring constant for the folded beam flexure as a result of lateral deflections can be found by combining forces and deflections of the beam segments resulting in:

$$k_x = \frac{200EI}{3L\delta_y^2}. \tag{23}$$

From this expression it can be easily seen that the spring constant in the x-direction decreases with increasing beam displacement in the y-direction. As a result the stiffness ratio also decreases with increasing lateral beam deflection. The total spring constant is a series connection of the lateral displacement dependent spring constant in equation (23) and the axial spring constant resulting from Hooke's law (11).

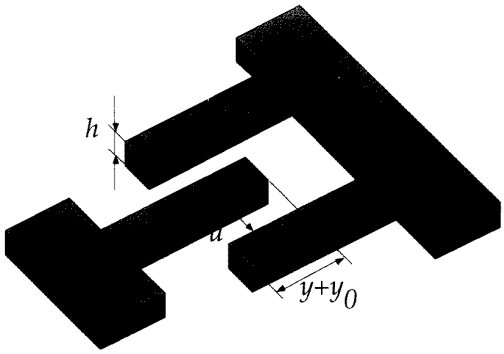

Figure 6. Cell of engaged comb finger arrays.

3. Electromechanical behaviour

3.1. Static behaviour

In the comb actuator a movable set (rotor) and a stationary set (stator) of comb fingers are engaged. A ground plane is located under the comb fingers which is normally connected to the same potential as the rotor in order to prevent electrostatic pull-down forces to the substrate. An engaged pair of fingers, being one cell, of a comb actuator is shown in figure 6. To simplify modelling the electrostatic field between the rotor and stator is approximated by a one-dimensional parallel-plate model between the engaged parts of the comb fingers. Therefore 3D effects like fringing fields, comb-finger end effects and the ground-plane levitation effect are neglected [24]. In our case these effects will lead to lateral electrostatic forces underestimated by about 5%, as will be discussed later.

3.1.1. Lateral deflection. The capacitance between the stator and the rotor can be expressed as:

$$C = \frac{2n\epsilon_0 b(y + y_0)}{d} \tag{24}$$

where n is the number of fingers, ϵ_0 is the dielectric constant in air, b is the width of the comb fingers, y_0 is the initial comb finger overlap, y is the comb displacement and d is the gap spacing between the fingers. In the case of voltage control the lateral electrostatic force in the y-direction is equal to the negative derivative of the electrostatic co-energy with respect to y:

$$F_{\mathrm{el}} = \frac{1}{2}\frac{\partial C}{\partial y}V^2 = \frac{n\epsilon_0 b}{d}V^2 \tag{25}$$

where V is the applied voltage between the stator and rotor. This force is acting on the spring to which the rotor is connected resulting in a deflection:

$$y = \frac{n\epsilon_0 b}{k_y d}V^2. \tag{26}$$

3.1.2. Side instability. Besides electrostatic forces along the y-axis, there are also electrostatic forces pulling the

stator and rotor fingers together. The electrostatic force in the axial direction is:

$$F_{\mathrm{el}} = \frac{n\epsilon_0 b(y+y_0)}{2(d-x)^2}V^2 - \frac{n\epsilon_0 b(y+y_0)}{2(d+x)^2}V^2. \qquad (27)$$

Normally the forces on both sides of the comb fingers cancel each other. However, when the first derivative of the electrostatic force with respect to x becomes larger than the restoring spring constant in the x-direction a side-instability of the comb drive is introduced. Hence stable comb operation is bounded by:

$$k_x > \left[\frac{\partial E}{\partial x}\right]_{x\to 0} = \frac{2n\epsilon_0 b(y+y_0)}{d^3}V^2. \qquad (28)$$

When the driving voltage exceeds the so-called side-instability voltage V_{SI} the comb drive becomes unstable leading to side sticking of the rotor and stator fingers. By combining equations (26) and (28) the voltage at which side-instability occurs can be expressed as:

$$V_{\mathrm{SI}}^2 = \frac{d^2 k_y}{2\epsilon_0 bn}\left(\sqrt{2\frac{k_x}{k_y}+\frac{y_0^2}{d^2}} - \frac{y_0}{d}\right). \qquad (29)$$

In this equation, the spring constant k_x refers to that in the deflected state, since side sticking occurs only when the comb is actuated (see (23)). By neglecting the second term in the root (when $k_x \gg k_y$), the maximum deflection y_{SI} that can be obtained before pull-in will occur is:

$$y_{\mathrm{SI}} = d\sqrt{\frac{k_x}{2k_y}} - \frac{y_0}{2}. \qquad (30)$$

From this equation it can be seen that the side-instability voltage and maximum deflection are proportional to the gap spacing and increase with the spring stiffness ratio. This shows that comb drive structures with small gap spacings are more susceptible to side instability [25] and that spring designs with a large stiffness ratio are preferred for large-deflection comb drive actuators. Other sources of instability may result from sideways pull-in of compliant fingers themselves and pull-in by the finger front ends when the stator and rotor are almost completely engaged [26]. Instabilities have to be avoided by proper design of the comb structure and flexure and supply together with maximum deflection, driving voltage and minimum feature size, the main constraints on comb actuator design. Large-deflection comb drive actuators at low driving voltages should employ compliant springs with a high stiffness ratio and a large number of comb fingers. In our comb-drive design, a folded flexure has been used which is connected at the centre to a beam that is able to hold a large number of comb fingers.

3.2. Dynamic behaviour

Using lumped elements the differential equation of motion is given by:

$$M_{eq}\ddot{y} + \alpha\dot{y} + k_y y = F_{el} = \frac{n\epsilon_0 b}{d}\left[V_P + v(t)\right]^2 \qquad (31)$$

where M_{eq} is the equivalent mass of the comb drive actuator, α is the equivalent viscous drag parameter, V_P is the DC polarisation voltage and $v(t)$ the AC voltage.

3.2.1. The fundamental frequency The fundamental frequency of the structure can be obtained from Rayleigh's quotient [23, 30]. Using the static deflection profile for the approximate fundamental mode shape function of the beams yields the following expression for the fundamental resonance frequency ω_0:

$$\omega_0 = \sqrt{\frac{k_y}{M_{shuttle} + \frac{1}{2}M_{truss} + \frac{96}{35}M_{beam}}} \qquad (32)$$

where the denominator of the fraction under the root sign resembles the equivalent mass M_{eq} in which $M_{shuttle}$ is the mass of the shuttle, M_{truss} is the mass of the single truss and M_{beam} is the mass of a single beam. The resonant frequency is ideally independent of V_P and $v(t)$.

3.2.2. Electric admittance—equivalent circuit If the comb drive is operated in a one-port configuration, the dynamic behaviour can be described by the electric admittance $Y(j\omega)$. The voltage is chosen as the independent variable because the electrodes define equipotential surfaces making the voltage independent of position. The constitutive equations of the electrostatic transducer, describing interactions between the mechanical and electrical variables can be expressed as:

$$\begin{bmatrix} \mathrm{d}q \\ \mathrm{d}F \end{bmatrix} = \begin{bmatrix} \frac{2n\epsilon_0 b(y_0+y_{00})}{d} & \frac{2n\epsilon_0 bV_P}{d} \\ -\frac{2n\epsilon_0 bV_P}{d} & k_y \end{bmatrix} \cdot \begin{bmatrix} \mathrm{d}u \\ \mathrm{d}y \end{bmatrix} \qquad (33)$$

where $\mathrm{d}q$ is the change in charge on the electrodes, $\mathrm{d}F$ is the change in electrostatic force, $\mathrm{d}u$ is the change in voltage, $\mathrm{d}y$ is the change in displacement and y_{00} denotes the static deflection caused by the polarisation voltage V_P. Combining (31) and (33a) the admittance is equal to:

$$Y(j\omega) = \frac{i}{v} = j\omega C_0 + \frac{j\omega C_1}{h(j\omega)} \qquad (34)$$

with

$$C_0 = \frac{2n\epsilon_0 b(y_0+y_{00})}{d} \qquad (35)$$

$$C_1 = \frac{4n^2\epsilon_0^2 b^2 u_0^2}{k_y d^2} \qquad (36)$$

$$H(j\omega) = \left(\frac{j\omega}{\omega_0}\right)^2 + \frac{j\omega}{Q\omega_0} + 1 \qquad (37)$$

where C_0 and C_1 denote the static and motional capacitance, respectively, and Q denotes the quality factor. An equivalent electrical circuit has been used to describe the electromechanical behaviour of the comb-drive actuator around the resonance frequency. This is shown in figure 7. The corresponding values of resistors, capacitors and inductors can be determined by parameter extraction from measured polar admittance characteristics [27].

4. Fabrication

Fabrication starts with a (100) p-type 3" silicon wafer. The first step is wet thermal oxidation at 1150 °C to obtain a 2 μm thick SiO_2 layer. Next a 5 μm thick polysilicon

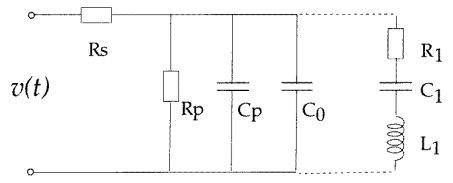

Figure 7. Equivalent circuit representation of the electrostatic comb-drive actuator including parasitic loads. $L_1 = 1/\omega^2 C_1$, $R_1 = 1/Q\sqrt{L_1/C_1}$, C_p = parasitic capacitance, R_p = parallel resistance, and R_s =series resistance (for C_1 see (36)).

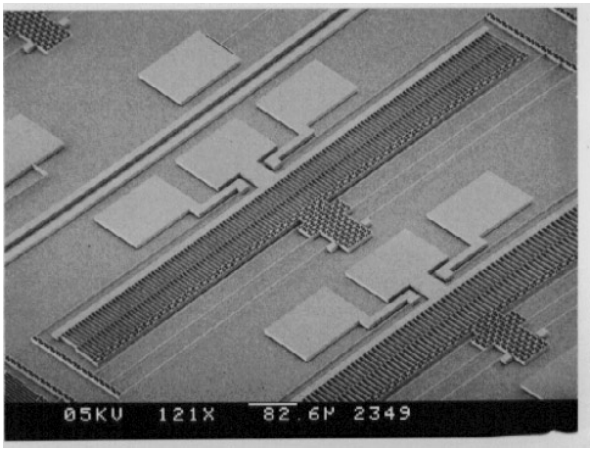

Figure 8. SEM photograph of fabricated comb-drive actuators. The total length of the actuator is about 1 mm.

layer is grown by LPCVD at a temperature of 590 °C, a pressure of 250 mTorr and a silane flow of 50 sccm. This polysilicon layer is heavily doped with boron by solid source indiffusion at 1100 °C for 3 hours. This yields a sheet resistance of about 4.5 Ω sq^{-1} and also results in a small residual strain and a strain gradient of the polysilicon layer. After boron indiffusion the BSG layer is stripped in a buffered HF solution. A 0.6 μm thick PECVD silicon oxide layer is grown which serves as an etch mask for the polysilicon. After patterning the silicon oxide by RIE using CHF_3 gas, the polysilicon is anisotropically etched using a SF_6, O_2, CHF_3 gas mixture [28]. After a cleaning step the sacrificial layer is etched for 50 minutes in a buffered HF solution. Drying by means of a cyclohexane freeze drying method prevents stiction of free structures to the substrate [29]. Finally a 1 μm thick aluminium layer is evaporated for backside contact. The final result is shown in figures 8 and 9.

5. Measurements

In the experiments both the substrate and the rotor electrode were connected to ground potential while the stator electrode was connected to a positive driving voltage. From static measurements flexure spring constants were determined and the Young's modulus of the boron doped polysilicon lateral to the wafer surface has been calculated. From dynamic measurements the resonance frequency

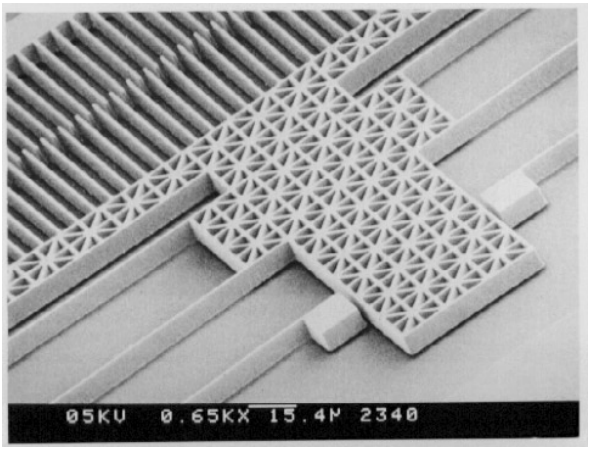

Figure 9. Close-up view showing the comb-finger array, the movable shuttle, the beam anchors and free-standing beams. A skeleton structure has been used to enhance sacrificial layer etching.

and quality factor are extracted using the equivalent circuit parameters. Dimensions were measured under a microscopy with a measurement error of ± 0.1 μm. Deflections were measured using a probe station with a microscopy and a micrometer eyepiece. The measurement error of this set-up was typically ± 0.2 μm.

5.1. Extraction of Young's modulus

The displacement as a function of the driving voltage was measured while applying a DC voltage between the rotor and the stator/substrate electrodes. Figure 10 shows the results for two crab-leg flexure designs. As expected the deflection is proportional to the voltage squared. If the number of comb fingers, finger thickness and gap spacing are known, the spring constant of the beams can be calculated from the slope of the deflection–voltage curves. The lateral Young's modulus of the polysilicon layer can be extracted from known beam dimensions using the measured spring constant. This yields a lateral Young's modulus of 160 ± 20 GPa for the polysilicon in our fabrication process. The large uncertainty in this value is mainly a result of the measurement error in the beam thickness. The Young's modulus is underestimated by a small factor because the electrostatic forces are somewhat larger as a result of fringing fields which have not been taken into account in our model. To obtain an indication of 3D effects, approximate expressions as derived by Johnson and Warne that include fringing fields and groundplane effects have been used [30]. For comb fingers with a height of 5 μm, a width of 2 μm, a gap spacing of 2 μm and a groundplane that is located 2 μm below the fingers, their expression yields an electrostatic force of: $F_{\mathrm{el}} = 2.6552 n \epsilon_0 V^2$. This approximated 3D force is about 5% larger than the parallel plate approximation. After correction for 3D effects a final value of 170 ± 20 GPa for the lateral Young's modulus was calculated. This value lies well within the range of reported values [1, 31] and is in good agreement with a theoretically calculated value of 164 GPa which has been obtained by

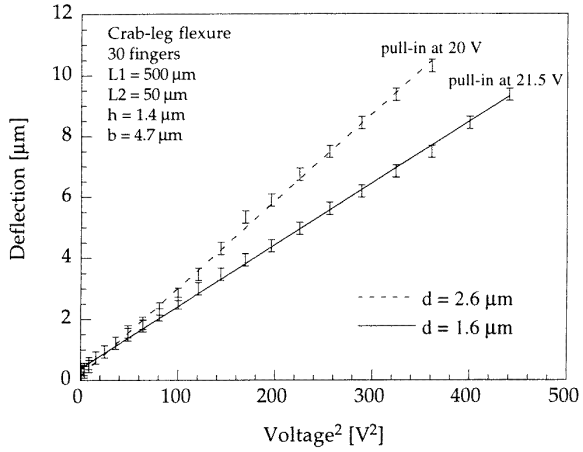

Figure 10. Measured deflection as a function of the driving voltage for two crab-leg flexure designs. The comb consisted of 30 fingers with a gap spacing d of 1.6 and 2.6 μm. The crab-leg structure consisted of a thigh segment of length L_1 of 500 μm and a shin of length L_2 of 50 μm. Measured beam width b was 4.7 μm and the beam thickness h was 1.4 μm.

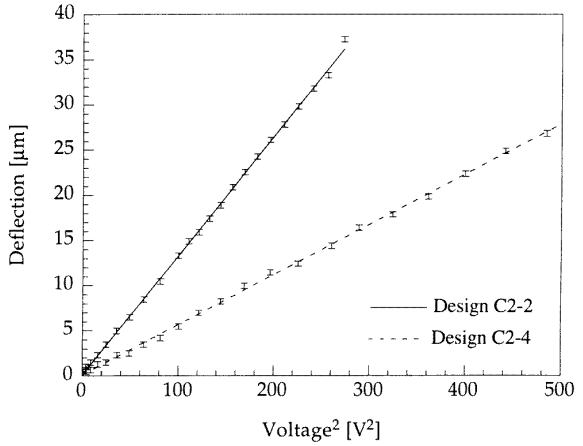

Figure 11. Measured deflection as a function of the driving voltage for several folded-flexure designs. Design C2-2, C2-4 employed comb structures with, respectively, 136 and 88 fingers. The gap spacing d equals 2.2 μm and the length of the beams in the folded flexure is 500 μm. The beam width b is 4.8 μm and the beam thickness h is 1.5 μm.

averaging well known mono-crystalline properties over the measured grain orientations in our polysilicon thin films.

The measured deflection-to-voltage behaviour of the folded-flexure actuator designs is shown in figure 11. The number of comb fingers in these designs has been increased resulting in lower driving voltages. Deflections of about 30 μm are obtained at driving voltages around 20 V.

5.2. Pull-in measurements

Another way to determine the static behaviour is by measuring the capacitance of the comb structure as a function of the DC bias voltage. Capacitance-to-voltage measurements have been performed using a HP4194A impedance analyser. The change in capacitance of some folded-beam designs is shown in figure 12. When the pull-in voltage is reached the comb drive becomes unstable and the capacitance suddenly changes as shown in the figure.

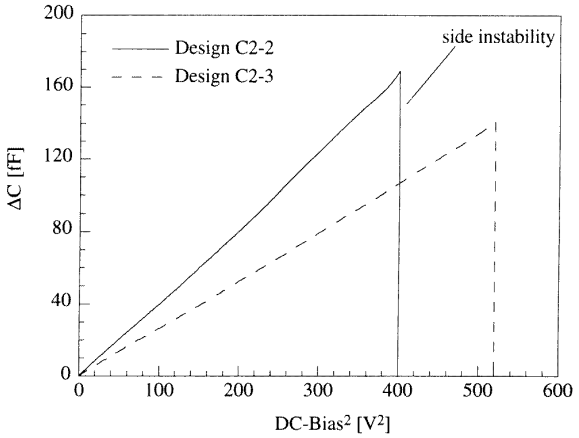

Figure 12. Capacitance change of folded-beam comb-drive designs as a function of the driving voltage squared. At a certain voltage pull-in of the comb structure occurs because of side instability. design C2-2 and C2-3 employed comb structures with, respectively, 136 and 105 fingers. Other parameters have already been given in figure 11.

Table 1. Measured pull-in voltage and deflection at pull-in for different comb-drive designs. The initial finger overlap y_0 is 4.6 μm, the gap spacing d is 2.2 μm, the width b of the structures is 4.8 μm and the thickness h of the beams is 1.5 μm.

Design	fingers	V_{pi} (V)	δ (μm)
C2-2	136	20.0	39.9
C2-3	105	22.8	39.9
C2-4	88	24.3	39.8
C2-5	74	26.1	39.7

The measured pull-in voltage and deflection at pull-in for different folded-flexure designs is summarised in table 1.

The spring constants of the beam in the x- and y-directions can be determined from these measurements; the measured spring constants k_x and k_y are, respectively, 17 N m^{-1} and 0.029 N m^{-1}. The theoretical values using measured dimensions and Young's modulus, are determined from equations (23) and (12), giving, respectively, $k_x = 19.2$ N m^{-1} and $k_y = 0.044$ N m^{-1}.

The measured spring constant along the y-axis is somewhat lower than the calculated value. The effect of the compliancy of the trusses, which have a thickness of 10 μm in our design, is very small, as calculated by using the expression for the spring constant derived by Judy [21]. More likely, the difference is a result of non-rectangular beam cross sections. Beams of width 4.8 μm, thickness at the bottom 1.5 μm and sidewalls inclined by only 0.1 μm from the bottom to the top will already have a spring

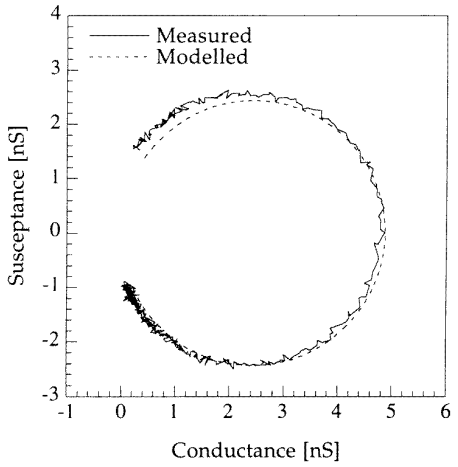

Figure 13. Measured and calculated admittance of comb actuator C2-2, having a beam length of 500 μm, a beam width of 4.8 μm, a beam thickness of 2 μm, a gap spacing of 2.2 μm and 136 comb fingers. The DC polarization voltage was equal to 15 V and the AC drive voltage was equal to 0.5 V. The broken curve is a theoretical curve using extracted parameter values: $C_0 + C_p$ = 414.5 fF, C_1 = 145.6 fF, L_1 = 68.4 kH, R_1 = 205 MΩ, R_p = 17.6 GΩ.

constant in the y-direction that is smaller by a factor of 2 than beams with a rectangular cross-section. Such a non-rectangular cross-section may easily result from some underetching during anisotropic etching of the structures.

The measured spring constant along the x-axis is in good agreement with the calculated value. A spring constant obtained directly from Hooke's law, (11), would result in a large overestimation of the spring constant in the x-direction yielding a theoretical value for k_x that is almost equal to 9000.

5.3. Frequency response

The admittance of the comb actuators was also measured using the HP 4194A impedance analyser. Figure 13 shows the measured and modelled polar admittance plot around the resonance frequency. Neglecting the series resistance R_s, which makes a small contribution compared with other admittances, the following parameter values were extracted from a best fit of the measured response: $C_0 + C_p$ = 414.5 fF, C_1 = 145.6 fF, L_1 = 68.4 kH, R_1 = 205 MΩ and R_p = 17.6 GΩ. This gives a resonance frequency $f \approx 1.60$ kHz and a quality factor $Q \approx 3.34$.

6. Position control

An important topic for further work is position control. In micropositioning, position feedback is desirable to reduce external disturbances and improve system response time and accuracy. In xy-stages, for example, springs are mechanically coupled and deflections in one direction may cause small but unwanted deflections in the orthogonal directions. A first study on feedback control of comb-drive actuators has already been carried out [32, 33]. The position can easily be obtained by measuring the capacitance of the comb drive itself. The capacitance of the comb drive can be measured by the superposition of a high frequency measurement signal on the drive signal. The measurement frequency needs to be much higher than the bandwidth of the system. In order to study control aspects it is convenient to consider the comb-drive actuator as a fourth-order system in order to obtain information about feedback limitations. The system is generally underdamped and to increase the system damping (stability) it is necessary to use, e.g., a P(I)D controller. Important aspects are that single comb drives can only be one-sided controlled and that the maximum driving voltage is limited by side-instability of the comb drive which put constraints on feedback control.

7. Conclusions

A large deflection, low-driving-voltage comb-drive actuator has been designed and fabricated by a one-mask fabrication process using boron doped polysilicon as the structural material and silicon dioxide as the sacrificial spacer. The lateral Young's modulus of the polysilicon layer has been obtained from static displacement-to-voltage measurements and is approximately 170 GPa. Theoretical lateral spring constants of clamped–clamped, crab-leg and folded-beam flexure designs have been determined, and the large deflection behaviour of these designs was investigated. Actuator behaviour is limited by electromechanical side instability, and expressions for the side-instability voltage and deflection are given. A one-port approach using electrostatic excitation and detection to generate and measure dynamic properties has been used. The electromechanical behaviour around the resonance frequency was described by an equivalent electric circuit. The modelled lateral spring constant of the folded-beam design as somewhat larger than experimentally determined values. This is likely to be a result of a non-rectangular cross section of the beams as a result of underetching. The theoretical axial spring constant of a folded beam which includes a reduction in spring constant with increasing lateral deflection was found to be in good agreement with experimental results in contrast to theoretical spring constants simply determined from Hooke's law. The electromechanical behaviour can be well described by the presented equivalent circuit which was used to extract the resonance frequency and quality factor from admittance measurements. An approach towards position control and feedback was briefly discussed.

Acknowledgments

The authors like to thank Bert Otter for making the SEM photographs and Theo de Vries for helpful discussions on system control. This research is sponsored by the Dutch Technology Foundation (STW).

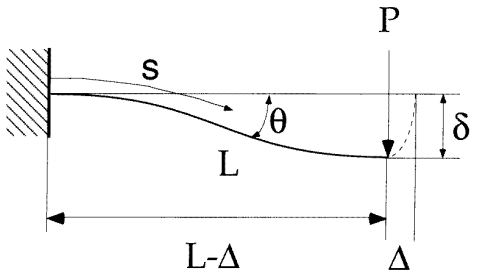

Figure A1. Sketch of clamped–guided beam including parameters.

Appendix A. Large deflection behaviour of a clamped–guided beam

In figure A1 a beam with one end fixed and the other guided in the x-direction is shown. When one of the ends of the beam is not constrained in the x-direction axial forces do not develop. In this case large deflection theory has to be applied and the differential equation that has to be solved is:

$$M = EI\frac{\mathrm{d}\theta}{\mathrm{d}s} = P(L - x - \Delta). \tag{A1}$$

Differentiating with respect to s gives:

$$\frac{\mathrm{d}^2\theta}{\mathrm{d}s^2} = -\frac{P}{EI}\frac{\mathrm{d}x}{\mathrm{d}s} = -\frac{P}{EI}\cos\theta. \tag{A2}$$

Integrating this equation results in:

$$\frac{1}{2}\left(\frac{\mathrm{d}\theta}{\mathrm{d}s}\right)^2 = -\frac{P}{EI}\sin\theta + C_i. \tag{A3}$$

The integration constant C_i can be found from the boundary condition, which is that the slope at the middle of the beam is maximal θ_0 from which follows

$$C_i = \frac{P}{EI}\sin\theta_0 \tag{A4}$$

yielding:

$$\frac{\mathrm{d}\theta}{\mathrm{d}s} = \sqrt{\frac{2P}{EI}\left(\sin\theta_0 - \sin\theta\right)}. \tag{A5}$$

The bar is assumed to be inextensible, in other words, it will not change its length during bending. Therefore:

$$\int_0^{\theta_0}\mathrm{d}s = \frac{1}{2}L. \tag{A6}$$

Combining equations (A5) and (A6), the following expression results:

$$\frac{1}{2}L\sqrt{\frac{2P}{EI}} = \int_0^{\theta_0}\frac{\mathrm{d}\theta}{\sqrt{\sin\theta_0 - \sin\theta}}. \tag{A7}$$

In order to bring the right side to the standard form of elliptic integrals a change in variables is introduced:

$$\sin\phi = \sqrt{\frac{1+\sin\theta}{1+\sin\theta_0}} \qquad p = \sqrt{(1+\sin\theta_0)/2}. \tag{A8}$$

After some manipulation this gives:

$$\frac{1}{2}L\sqrt{\frac{P}{EI}} = \int_{\phi_1}^{\pi/2}\frac{\mathrm{d}\phi}{\sqrt{1-p^2\sin^2\phi}} \qquad \phi_1 = \arcsin\ {}^{-1/2}\sqrt{2p^2}. \tag{A9}$$

This equation has one unknown, the modulus p, which can be found by trial and error and numerically solving the integral. Since $\mathrm{d}y = 2\mathrm{d}s\sin\theta$, the vertical deflection is given by:

$$\delta = 2\sqrt{\frac{EI}{2P}}\int_0^{\theta_0}\frac{\sin\theta\,\mathrm{d}\phi}{\sqrt{\sin\theta_0 - \sin\theta}}. \tag{A10}$$

Using the same substition as before:

$$\delta = 2\sqrt{\frac{EI}{P}}\int_{\phi_1}^{\pi/2}\frac{(2p^2\sin\phi - 1)\mathrm{d}\phi}{\sqrt{1-p^2\sin\phi}}. \tag{A11}$$

The expression for the deflection of a cantilever beam loaded at the tip can be obtained in the same way and is given by:

$$\delta = \sqrt{\frac{EI}{P}}\int_{\phi_1}^{\pi/2}\frac{(2p^2\sin\phi - 1)\mathrm{d}\phi}{\sqrt{1-p^2\sin\phi}} \tag{A12}$$

where p can be found from:

$$\sqrt{\frac{PL^2}{EI}} = \int_{\phi_1}^{\pi/2}\frac{\mathrm{d}\phi}{\sqrt{1-p^2\sin^2\phi}}. \tag{A13}$$

References

[1] Tang W C, Nguyen T C and Howe R T 1989 Laterally driven polysilicon resonant microstructures *Sensors Actuators* **20** 25–32

[2] Brenner R A, Pisano A P and Tang W C 1990 Multiple mode micromechanical resonators *Proc. IEEE Micro Electro Mech. Syst. (Napa Valley, CA 1990)* pp 9–14

[3] Judy M W and Howe R T 1993 Polysilicon hollow beam lateral resonators *Proc. IEEE Micro Electro Mech. Syst. (Fort Lauderdale, FL, 1993)* pp 265–71

[4] Lin L, Nguyen C T C, Howe R T and Pisano A P 1992 Micro-electromechanical filters for signal processing *Proc. IEEE Micro Electro Mech. Syst. (Travemünde, Germany, 1992)* pp 226–31

[5] Jaecklin V P, Linder C, de Rooij N F, Moret J M and Vuilleumier R 1993 Optical microshutters and torsional micromirrors for light modulator arrays *Proc. IEEE Micro Electro Mech. Syst. (Fort Lauderdale, FL, 1993)* pp 124–7

[6] Tabata O, Asahi N, Fujitsuka N, Kimura M and Sugiyama S 1993 Electrostatic driven optical chopper using SOI *Proc. 7th Conf. Solid-State Sens. Actuators, Transducers '93 (Yokohama, Japan, 1993)* pp 124–7

[7] Chen P Y and Muller R S 1994 Microchopper-modulated IR microlamp *Proc. IEEE Solid-State Sens. Actuators Workshop (Hilton Head Island, SC, 1994)* pp 239–42

[8] Kim C J, Pisano A P and Muller R S 1992 Overhung electrostatic micro gripper *J. Microelectromech. Syst.* **1** 31–6

[9] Loconto D P and Muller R S 1993 High-sensitive micromechanical electrostatic voltmeter *Proc. 7th Int. Conf. Solid-State Sens. Actuators, Transducers '93 (Yokohama, Japan, 1993)* pp 878–81

[10] Lee A P and Pisano A P 1992 Polysilicon angular microvibromotors *J. Microelectromech. Syst.* **1** 70–6
[11] Garcia E J and Sniegowski J J 1995 Surface micromachined microengine as the driver for micromechanical gears *8th Int. Conf. on Solid-State Sens. Actuators, Transducers '95 (Stockholm, Sweden, 1995)* pp 365–8
[12] Jaecklin V P, Linder C, de Rooij N F, Moret J M, Bischot R and Rudolf F 1992 Novel polysilicon comb actuators for xy-stages *Proc. IEEE Micro Electro Mech. Syst. (Travemünde, Germany, 1992)* pp 147–9
[13] Jaecklin V P, Linder C and de Rooij N F 1993 Comb actuators for xy-microstages *Sensors Actuators* **A39** 83–9
[14] Jansen H, Verhagen R and Elwenspoek M 1994 The black silicon method III: design rules, modelling, optimisation and performance of precision position systems for scanning probe, gripping and other MEMS applications *Seminar on Handling and Assembly of Microparts (Vienna, Austria, 1994)*
[15] Brugger J, Jaecklin V P, Linder C, Blanc N, Indermühle P F and de Rooij N F 1993 Microfabricated tools for nanoscience *J. Micromech. Microeng.* **3** 161–7
[16] Xu Y, Miller S A and MacDonald N C 1995 Microelectromechanical scanning tunneling microscope *Proc. 8th Int. Conf. Solid-State Sens. Actuators, Transducers '95 (Stockholm, Sweden,)* pp 640–3
[17] Pisano A P and Cho Y H 1990 Mechanical design issues in laterally-driven microstructures *Sensors Actuators* **A21–A23** 1060–4
[18] Gere J M and Timoshenko S P 1987 *Mechanics of Materials* 2nd edn (Van Nostrand Reinhold)
[19] Frisch-Fay R 1962 *Flexible bars* (London: Butterworths)
[20] Tang W C 1990 Electrostatic comb drive for resonant sensor and actuator applications *PhD Thesis* Department of Electrical Engineering and Computer Sciences, University of California, Berkeley, CA
[21] Judy M W 1994 Micromechanisms using sidewall beams *PhD Dissertation* Faculty of Electrical Engineering and Computer Sciences, University of California, Berkeley, CA
[22] Fedder G K 1994 Simulation of microelectromechanical systems *PhD Dissertation* Faculty of Electrical Engineering and Computer Sciences, University of California, Berkeley, CA
[23] Shames I H and Dym C L 1985 *Energy and Finite Element Methods in Structural Mechanics* (New York: McGraw-Hill)
[24] Tang W C, Lim M G and Howe R T 1992 Electrostatic comb drive levitation and control method *J. Microelectromech. Syst.* **1** 170–8
[25] Hirano T, Furuhata T, Gabriel K J and Fujita H 1992 Design, fabrication and operation of sub-micron gap electrostatic comb-drive actuators *J. Microelectromech. Syst.* **1** 52–9
[26] Jaecklin V P, Linder C, de Rooy N F and Moret J M 1992 Micromechanical comb actuators with low driving voltage *J. Micromech. Microeng.* **2** 250–5
[27] Tilmans H A C 1993 Micromechanical sensors using encapsulated built-in resonant strain gauges *PhD Dissertation* Faculty of Electrical Engineering, University of Twente, Enschede, The Netherlands
[28] Legtenberg R, Jansen H, de Boer M and Elwenspoek M 1995 Anisotropic reactive ion etching of silicon using $SF_6/O_2/CHF_3$ gas mixtures *J. Electrochem. Soc.* **142** 2020–8
[29] Legtenberg R 1996 Electrostatic actuators fabricated by surface micromachining techniques *PhD Thesis* University of Twente, Enschede, The Netherlands
[30] Johnson W A and Warne L K 1995 Electrophysics of micromechanical comb actuators *J. Microelectromech. Syst.* **4** 49–59
[31] Pratt R I, Johnson G C, Howe R T and Chang J C 1991 Micromechanical structures for thin film characterization *Proc. Int. Conf. on Solid-State Sens. Actuators, Transducers '91 (San Francisco, CA, 1991)* pp 205–8
[32] Groeneveld A W 1995 Electromechanical behaviour and study towards position control of electrostatic comb drive actuators *Master Thesis* University of Twente, Enschede, The Netherlands
[33] Legtenberg R, Groeneveld A W and Elwenspoek M 1995 Towards position control of electrostatic comb drives *Proc. 6th Workshop Micromachin. Micromech. Microsyst., MME '95 (Copenhagen, Denmark, 1995)* pp 124–7